coatings

MDPI

Article

Human Teeth Disease Detection Using Refractive Index Based Surface Plasmon Resonance Biosensor

Mohammad Khursheed Alam [1,*], Vigneswaran Dhasarathan [2,3], Ayyanar Natesan [4], Ramanujam Nambi [5], Mahmud Uz Zaman [6], Kiran Kumar Ganji [1], Rehana Basri [7], Manay Srinivas Munisekhar [1], Anil Kumar Nagarajappa [8] and Huda Abutayyem [9]

1 Preventive Dentistry Department, College of Dentistry, Jouf University, Sakaka 72345, Saudi Arabia
2 Department of Electronics and Communication Engineering, KPR Institute of Engineering and Technology, Coimbatore 641407, India
3 Centre for IoT and AI (CITI), KPR Institute of Engineering and Technology, Coimbatore 641407, India
4 Department of Electronics and Communication Engineering, Thiagarajar College of Engineering, Madurai 625015, India
5 Department of Physics, K.L.N. College of Engineering, Chennai 630611, India
6 Oral and Maxillofacial Surgery and Diagnostic Sciences Department, College of Dentistry, Prince Sattam Bin Abdulaziz University, Al-Kharj 16245, Saudi Arabia
7 Department of Internal Medicine, College of Medicine, Jouf University, Sakaka 72345, Saudi Arabia
8 Oral Medicine & Radiology Division, Department of Oral & Maxillofacial Surgery & Diagnostic Sciences, College of Dentistry, Jouf University, Sakaka 72345, Saudi Arabia
9 Department of Clinical Sciences, Center of Medical and Bio-Allied Health Sciences Research, College of Dentistry, Ajman University, Ajman 346, United Arab Emirates
* Correspondence: mkalam@ju.edu.sa

check for updates

Citation: Alam, M.K.; Dhasarathan, V.; Natesan, A.; Nambi, R.; Zaman, M.U.; Ganji, K.K.; Basri, R.; Munisekhar, M.S.; Nagarajappa, A.K.; Abutayyem, H. Human Teeth Disease Detection Using Refractive Index Based Surface Plasmon Resonance Biosensor. *Coatings* **2022**, *12*, 1398. https://doi.org/10.3390/coatings12101398

Academic Editor: Arūnas Ramanavičius

Received: 24 August 2022
Accepted: 22 September 2022
Published: 25 September 2022

Abstract: The paper proposes a surface plasmon resonance (SPR) biosensor utilizing MXene and a Molybdenum Disulfide (MoS_2) material layer, placed on the Ag metal-based conventional biosensor to detect disease in human teeth. The SPR biosensor works on the principle of attenuated total reflection. The transverse matrix method was utilized for the reflectivity calculation. The thickness of the Ag layer, MXene, and MoS_2 were taken as 45, 0.993, and 0.375 nm, respectively. Single-layer MoS_2 and two layers of MXene were taken, and the highest sensitivity of the sensor for the enamel, dentin, and cementum was obtained at 83.219 deg/RIU, 91.460 deg/RIU, and 104.744 deg/RIU. MoS_2 was used to enhance the biocompatibility of the analyte with the sensing layer. The aqueous solution had been considered as sensing medium.

Keywords: human dental disease detection; sensitivity improvement; MoS_2; MXene; biosensor

1. Introduction

For decades, surface plasmon-based biosensors have been employed in biochemical sensing. They are suitable for sensing-based applications due to their qualities such as dependability, label-free detection, increased sensitivity, and immediate detection capabilities [1–3]. SPR biosensors based on prisms [4], optical fibres [5], and Bragg gratings [6] have been implemented. Based on the attenuated total reflection (ATR) phenomena [7,8], Kretschmann proposed a prism-based configuration [9]. In this configuration, a layer of metal has been placed over the prism (also known as a traditional biosensor). At the prism-metal contact in this configuration, the transverse magnetic (TM) polarised input wave generates evanescent waves. These waves decay exponentially at the metal prism interface [10]. Finally, a surface plasmon is generated at the metal-prism interaction. Due to the formation of large surface plasmons, a change in the RI of the sensing medium produces a shift in the resonance angle [11]. The performance characteristics of the traditional biosensor setup (Kretschmann's configuration) are poor. 2D materials are placed between the metal and the sensing layer to increase the biosensor's performance [12]. Besides

SPR biosensors, other optical devices such as metal-dielectric-metal (MDM) waveguide structures have also gained a lot of attention among different plasmonic guiding structures. This is due to its features of sustaining zero-bend, deep subwavelength modes with the ease of fabrication and losses [13,14].

Besides conventional caries detection methods, some other methods used to detect diseases in human teeth include: diagnodent, electrical caries monitor (ECM), Fiber-optic Transillumination (FOTI), Digital Imaging Fiber-optic Transillumination (DIFOTI), Quantitative Light Induced Fluorescence (QLF), digital radio graphs, etc. [15]. These detection methods have been tabulated in Table 1, demonstrating their advantages and disadvantages. Proposed SPR biosensor can diagnose common diseases of the oral cavity. It has great potential for the clinical diagnosis of early dental caries. Dental caries is the most prevalent chronic disease worldwide.

Table 1. Advantages and disadvantages of some detection methods for human teeth disease detection.

Detection Methods	Classification	Advantages	Disadvantages
Diagnodent	Point techniques (dental caries)	Trouble-free and rapid test, accurate, flexible, and mobile operated	In order to give a treatment plan, the laser device Diagnodent cannot determine the degree of demineralization.
ECM		Helps dentists to monitor, demineralize, and treat patients' root caries lesions, as well as assists in a thorough examination of the tooth's structural details.	Its performance relies upon a tooth's temperature, tissue width, hydration, and surface area of the material.
FOTI	Light property technique	Compact and battery-operated devices, observations of cusp fractures and cracked teeth, and diagnoses of early carious lesion	Moderate sensitivity (85%) and specificity are around 99%, detects only the occlusal caries on premolars and molars teeth.
DIFOTI		Diagnosis in real-time, greater sensitivity for early lesions detection.	Its camera is very heavy. Fitting inside a younger person's mouth is a complex process.
QLF	Light emitting devices	User friendly, easily fits inside children's mouths, etc.	The light source used is a laser, size is bulky.
Digital Radiographs	Radio graphs	Real time analysis, rapid method so it saves time and is also quite cheaper.	Can be dangerous to humans because it uses ionizing radiation, width, and rigidity.

MoS_2 has a great 1.8 eV band gap, a high absorption efficiency of 6%, and a broad 5.1 eV work function [16–18]. Due to its hydrophobic nature, MoS_2 has a high affinity for absorbing biomolecules, which can be used in biological sensing [19] and used as a protective layer for the metal's oxidation [20,21]. According to various studies, work has been performed on the design of SPR sensors based on graphene, BP, and transition metal dichalcogenides (TMDCs) materials [22–24]. BP-MoS_2 materials are used as the primary 2D material in the SPR biosensor that Srivastava and Jha described, which has a sensitivity of 110 deg/RIU [25]. Singh and Raghuvanshi proposed a gas detection SPR sensor with a sensitivity of 245.5 deg/RIU using a bi-Au layer and BP layers [26]. A biosensor with a sensitivity of 279 deg/RIU had been proposed by Wu et al. The proposed design contained graphene, black phosphorus, and Au as a metal layer [27]. A gold grating over gold-aluminium metal layers was used to build a 279.6 deg/RIU sensitivity SPR biosensor by Bijalwan et al. [28]. Karki et al. proposed a biosensor with 352 deg/RIU sensitivity, consisting of franckeite nanosheets and nickel and silver metal films [29]. Liu et al. developed an SPR biosensor based on a tilted fibre Bragg grating (TFBG) for the detection of environmental estrogens (EEs) [30]. The idea of a pressure sensor was first out by Sun et al. Their main findings included the device's 45 ms reaction time and 14,000 cycles of astonishing cyclic repeatability [31]. Du et al. proposed a reliable optical fibre-based photodetector, based on vertical ZnO-P3HT heterostructure to accomplish a self-powered and ultra-fast UV sensing [32]. They were able to obtain a response and recovery time of under 40 milliseconds and a customizable photo response. A gas sensor based on the ZnO-Bi_2O_3 structure was introduced by Liu et al. and may be used to identify diabetes early on [33]. Shangguan et al. and Wu et al. proposed RI-based absorption sensors and attained greater terahertz absorption rates [34,35]. MXene is a new emerging 2D material that has recently gained popularity among researchers due to its electrical properties, such as high conductivity, and optical properties such as the ability to easily access hydrophilic surfaces [36,37], greater spacing between interlayers, higher thermal stability, and surface area [38]. It features a hexagonal crystal structure with optical qualities, such as bandgap correction, increased light, and matter interactions. $M_{n+1}X_nT_x$ is the generic formula, with M, X_n, and T_x being transition metals, C or/and N, where n is an integer between 1 and 3, and surface functional groups, respectively [39]. MXene has previously been used in sensing-based applications such as gas, electrochemical, etc. Other uses included energy storage, water purification, photo detector, and chemical catalysts, etc.

Since the sensor reports greater sensitivity, Ag was the favoured plasmonic metal in the SPR sensor [40,41]. The primary disadvantage of silver was that it oxidised easily, which may be mitigated to a higher amount using the sensor's bimetallic layer [42,43]. The Au-prism-based SPR sensor had limited sensitivity to the analyte since gold had superior chemical stability but a low capacity to bind molecules [44]. Another disadvantage of Au metal-based sensors was that their SPR curves were broader. As a result, measuring sensitivity accurately was difficult, and the full width half maximum (FWHM) parameter was large.

The following is how the manuscript is organized: Section 2 describes the biosensor's suggested design. The results and discussions are reported in Section 3. Section 4 brings the proposed work to a close.

2. Proposed Structure and Design Methodology

As illustrated in Figure 1, the suggested sensor is comprised of three layers, with the SF11 prism acting as the foundation material. The He-Ne laser source had been used as the optical source [45]. After the input wave was reflected from the prism-metal contact in the output portion, the signal was received by a photodetector. Due to its high RI [42], the SF11 prism was an excellent candidate. The sensor design consisted of a silver (Ag) layer thickness of $d_2 = 45$ nm above the prism base, followed by layers of MoS_2 and MXene with $d_3 = P * 0.375$ nm $d_4 = G * 0.993$ nm, respectively. The sensing layer was where bio-molecular interactions between immobilized ligands and analytes occurred. Enamel, dentin, and cementum have refractive indexes of 1.631, 1.540, and 1.582, respectively [43].

Using the Sellmeier equation, the coupling prism's RI is expressed as [46]:

$$n_{prism} = \left(\frac{\alpha_1 \lambda^2}{\lambda^2 - \beta_1} + \frac{\alpha_2 \lambda^2}{\lambda^2 - \beta_2} + \frac{\alpha_3 \lambda^2}{\lambda^2 - \beta_3} + 1 \right)^{1/2} \tag{1}$$

The constants α_1, α_2, α_3 have the values 1.73759695, 0.313747346, and 1.89878101, respectively, and other constants β_1, β_2 and β_3 have values 0.013188707, 0.0623068142 and 155.23629, respectively. The RI of silver metal is calculated by the formula [47]:

$$n_{Ag} = \left(1 - \frac{\lambda^2 * \lambda_c}{\lambda_p^2 (\lambda_c + \lambda * i)} \right)^{1/2} \tag{2}$$

where the λ_c is the collision wavelength whose value is equal to 8.9342×10^{-6} m, and λ_p is the plasma wavelength whose value equals 1.6826×10^{-7} m [45]. The other layers (MoS_2 and MXene) RI are taken as $5.0805 + 1.1723 * i$ and $2.38 + 1.33 * i$, respectively, at 633 nm.

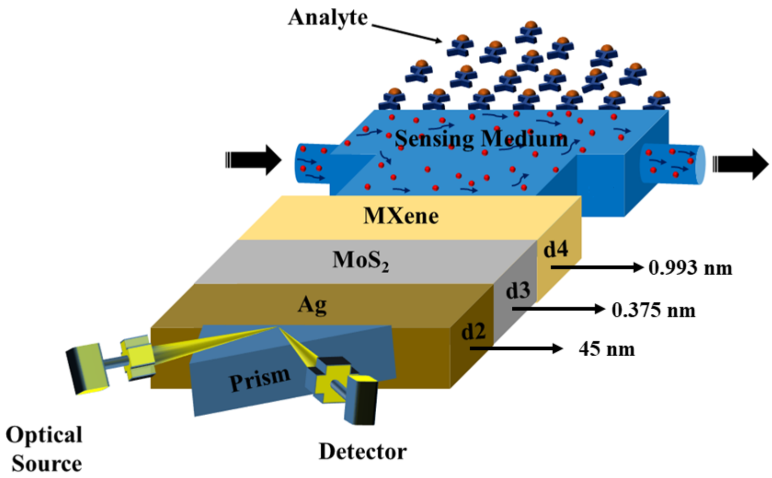

Figure 1. Sensor diagram.

The problem of indigestion is caused if we do not chew food properly. Therefore, as a concern, its early detection of dental caries is necessary. Although these are the suspended particles, and a small amount (concentration) of the enamel, dentin and cementum particles are added to the sensing layer for the sensing purpose; the sensing layer's RI changes. The biochemical reaction process occurs between the enamel, dentin, and cementum and water, changing the RI of the solution as the concentration of these particles is added. This RI change can be mathematically expressed as:

$$\Delta n_s = n_s^2 - n_s^1 = C\frac{\delta n}{\delta c}, \tag{3}$$

$$\text{here } n_s^2 = n_s^1 + C\frac{\delta n}{\delta c}, \text{ here } C \text{ represents the concentration of particles added.} \tag{4}$$

The n_s^2 and n_s^1 represents RI of the sensing layer after the particle's adsorption and RI of the solution before adding the particles into the sensing layer. Let us consider 100 nM of the molecular particle concentration has been added into the sensing layer, i.e., $C = 100$ nM. The fraction $\frac{\delta n}{\delta c}$ indicates the increasing value of RI due to the inclusion of the particles. This increment parameter value of RI is $\frac{\delta n}{\delta c} = 0.182$ cm^3/g. The propagation constant of surface plasmon wave (SPW) alters with alteration in SPR angle given by [48]:

$$k_S = \frac{2\prod}{\lambda}\mu_p sin\theta_{SPR} \tag{5}$$

The reflectance computation without approximation was completed by the transfer matrix method. An N-layer structure was defined using a characteristics matrix shown here:

$$S = \prod_{X}^{N-1} S = \begin{bmatrix} S_{11} & S_{12} \\ S_{21} & S_{22} \end{bmatrix} \tag{6}$$

$$\text{as } S_X = \begin{bmatrix} cos\beta_x & -isin\left(\frac{\beta_x}{q_x}\right) \\ -iq_x sin\beta_x & cos\beta_x \end{bmatrix} \tag{7}$$

where, S_X is the X^{th} layer matrix, and β_x and q_x are the optical admittance and phase factor, respectively.

$\beta_x = \frac{2\pi}{\lambda} d_x \sqrt[2]{\epsilon_x - n_1^2 sin^2\theta_1}$ and $\frac{q_x = \sqrt[2]{\epsilon_x - n_1^2 sin^2\theta_1}}{\epsilon_x}$

θ_1 denotes the incident angle and ϵ_x denotes the dielectric constant.

The reflection coefficient for the p-polarized wave has been calculated by:

$$R_p = |r_p|^2 = \left(\frac{(S_{11} + S_{12}q_N)q_1 - (S_{21} + S_{22}q_N)}{(S_{11} + S_{12}q_N)q_1 + (S_{21} + S_{22}q_N)} \right) \tag{8}$$

The performance parameters are used to describe an SPR sensor's performance. Sensitivity (S), detection accuracy (DA), full width half maximum (FWHM), and figure of merit are crucial performance characteristics (FOM). The maximum values for S and DA should indicate that the suggested sensor is performing satisfactorily. The FWHM value should be as low as possible. $S = \frac{\Delta\theta_R}{\Delta n}$ is the formula for an SPR sensor's sensitivity calculation. Degree/RIU is its unit. It can be characterised as the change in the resonance angle ($\Delta\theta_R$) in relation to the change in the RI of the sensing medium (Δn). The SPR curve is used to calculate this factor. When DA = 1/FWHM, the detection accuracy is calculated. It has the degree: 1 unit. The SPR curve is used to calculate this factor. The mathematical formula for the full-width half maxima (FWHM) is FWHM $= \theta_b - \theta_a$, and the unit is degree. This parameter provided information about the reflectance curve's width and sharpness. The Figure of Merit (FOM) was written as $FOM = S * DA$. RIU^{-1} is its unit. FOM represented the SPR sensor's resolution.

2.1. Numerical Modelling

As demonstrated in this research, the proposed model was created and evaluated using a numerical simulation based on the finite element technique (FET). In order to simulate the given model, we simulated the 2D geometry of the suggested sensor using COMSOL Multiphysics version 5.5. The suggested (BK7/ Ag/ MoS_2/ MXene) SPR biosensor is shown in Figure 2b, with a light source incident at a 633 nm wavelength on the top of prism BK7. Once more, the periodicity boundary conditions and periodic port conditions (indicated in red in Figure 2) were applied [49]. A very fine physics-controlled sized mapped mesh with elements as small as 5×10^{-5} µm and as large as 0.025 µm had been selected for this FEM model, as seen in Figure 2a. Additionally, we used the parametric sweep operation to carry out the angular interrogation technique, while altering the incident angle of the source. With an incremental deviation of 0.1 degrees, the incident angle had been simulated from 53 to 90 degrees. The reflectance intensity for each entering angle was calculated to obtain the resonance angle. Then, by examining the minimum reflectance intensity at the output, the resonance angle was ascertained from the output intensity curve. The frequency-domain solver was used to solve the model at a frequency of $3 \times 10^8/\lambda$ Hz.

The shift in the output reflection intensity curve for the analyte layer refractive index fluctuation was calculated to determine the sensors sensitivity and performance. In order to show the suggested model in SPR circumstances, we also displayed the electric field strength and magnetic field propagation at the resonance angles, as shown in Figure 3. Due to the intense localization and maximal excitations of surface plasmons in the plasmonic layer, the electric field and magnetic field were increased in the resonance state [50,51]. When resonance was present, as shown in Figure 3, the plasmonic gold layer showed an increased electric field intensity.

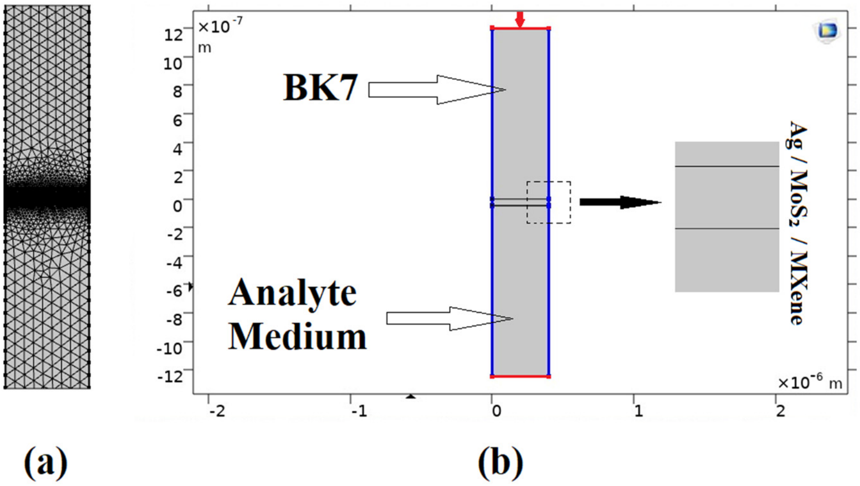

Figure 2. COMSOL Multiphysics design layout for the proposed (BK7/ Ag/ MoS_2/ MXene) SPR biosensor: (**a**) The field of computational meshing; (**b**) A simulation-based model for the proposed structure.

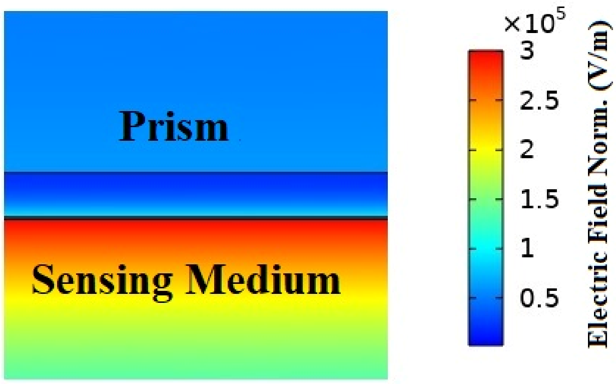

Figure 3. The electric field normal distribution and magnetic field propagation of the suggested hybrid (BK7/ Ag/ MoS_2/ MXene) SPR biosensor structure are as follows: On the surface of gold, the distribution of the electric field exhibits an amplified field at a resonance angle.

2.2. Field Distribution Computation

The field distribution of the input TM polarised wave within each layer for the proposed SPR sensor provided information about the augmentation of the evanescent field under various circumstances. The generation of the evanescent field over the analytical interface was crucial for the SPR phenomena. It is due to this that the analytes interface was where the sensing was completed. The distribution of the field components with the top layer was defined by the overall characteristics matrix. Its expression is [52]:

$$\begin{bmatrix} H_{y1}(z) \\ -E_{x1}(z) \end{bmatrix} = P_1(z) \cdot \begin{bmatrix} 1 + r_p \\ q_1(1 - r_p) \end{bmatrix} H_y^{inc}, z_1 \leq z \leq z_2 \tag{9}$$

where, $H_{y1}(z)$, $E_{x1}(z)$ denotes the magnetic and electric fields, respectively.

H_y^{inc} denotes the incident magnetic field amplitude and r_p denotes the reflection coefficient.

$$\text{where, } P_1(z) = \begin{bmatrix} \cos\left(\beta_{k(\text{at } z)}\right) & i/q_1 \sin\left(\beta_{k(\text{at } z)}\right) \\ iq_1 \sin\left(\beta_{k(\text{at } z)}\right) & \cos\left(\beta_{k(\text{at } z)}\right) \end{bmatrix} \tag{10}$$

Next, these field distributions within the layer $j \geq 2$ are given by:

$$\begin{bmatrix} H_{yj}(z) \\ -E_{xj}(z) \end{bmatrix} = P_j(z) * \prod_{j-1}^{1} P(z = z_i + d_i) * \begin{bmatrix} 1 + r_p \\ q_j(1 - r_p) \end{bmatrix} H_y^{inc}, z_j \leq z \leq z_{j+1} \quad (11)$$

$$\text{where, Propagation matrix, } P_j(z) = \begin{bmatrix} \cos\left(\beta_{k(at\ z=z-1)}\right) & i/q_j \sin\left(\beta_{k(at\ z=z-1)}\right) \\ iq_j \sin\left(\beta_{k(at\ z=z-1)}\right) & \cos\left(\beta_{k(at\ z=z-1)}\right) \end{bmatrix} \quad (12)$$

3. Results and Discussion

The sensitivity of a biosensor with a modified Kretschmann configuration that included MoS_2 and graphene is discussed here in this section. The transfer matrix method was used to create reflectance curves that demonstrated how the reflectivity of light changed with incident angle. Figure 4A showed the conventional sensor design, $M = 0,\ \ G = 0$. Figure 4B,C demonstrated the modified conventional designs with layer combinations $M = 0,\ \ G = 1$, and $M = 1,\ \ G = 0$, and Figure 4D gave the reflectance spectra for the proposed sensor design ($M = 1,\ \ G = 1$). The RI range of sensing media varies from 1.33 to 1.631. For Figure 4A–D, the values of minimum reflectance and change in SPR angle ($\Delta\theta$) calculated have been shown in Table 2.

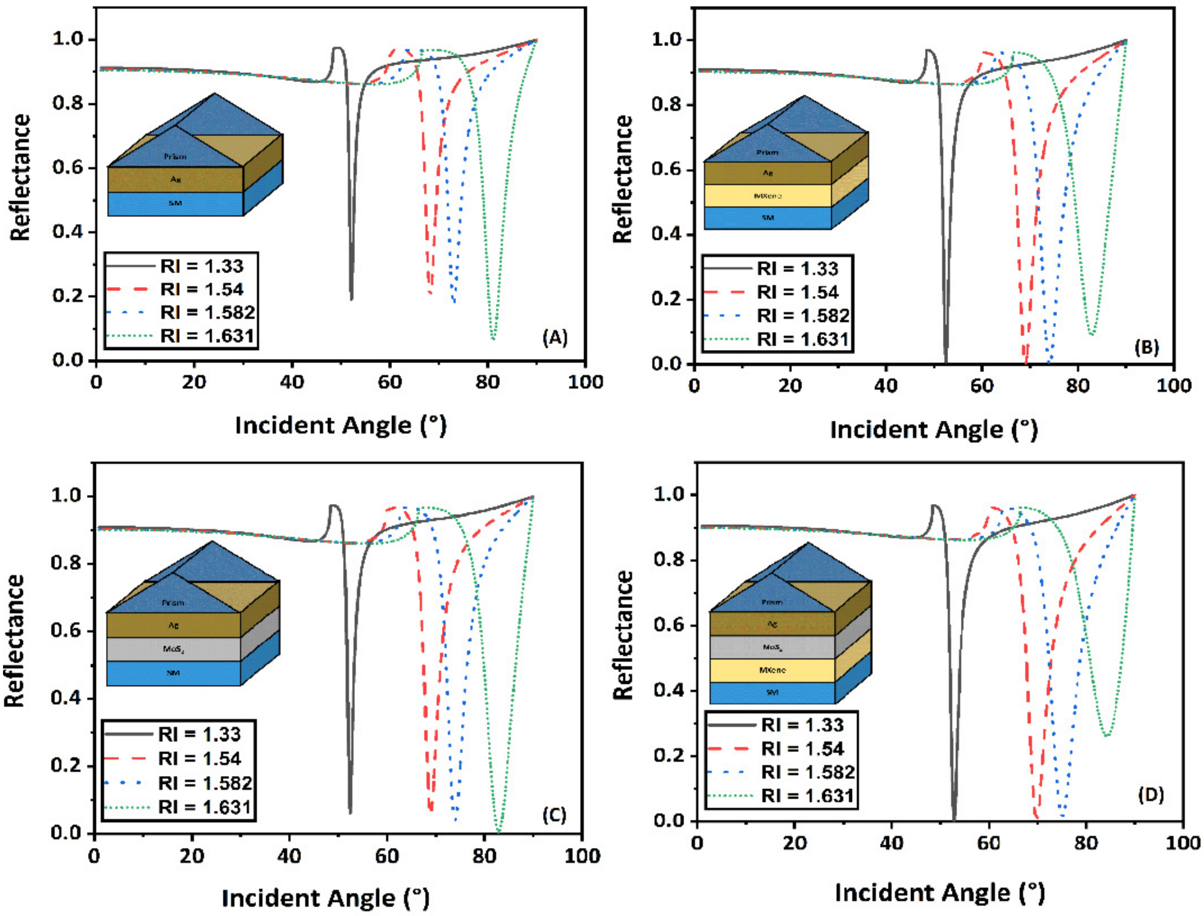

Figure 4. Change in reflectance with incident angle for different RI of sensing medium (**A**) $M = 0,\ G = 0$, (**B**) $M = 0,\ \ G = 1$, (**C**) $M = 1,\ \ G = 0$, and (**D**) $M = 1,\ \ G = 1$.

Table 2. Computed minimum reflectance and change in SPR angle values.

RI	Layers	Min. Reflectance	Δθ (deg)
1.33	$M = 0,\ G = 0$	0.19109	
1.54		0.19935	16.104
1.582		0.17701	20.896
1.631		0.06476	28.988
1.33	$M = 0,\ G = 1$	0.19109	
1.54		0.19935	16.534
1.582		0.17701	21.566
1.631		0.06476	30.382
1.33	$M = 1,\ G = 0$	0.06071	
1.54		0.05924	16.498
1.582		0.04069	21.521
1.631		0.00521	30.473
1.33	$M = 1,\ G = 1$	0.000711776	
1.54		0.00488	16.967
1.582		0.01825	22.263
1.631		0.26247	31.446

As a result, we may infer that adding one MoS_2 and one MXene layer to our biosensor greatly increased its sensitivity, compared to the current design. To better understand how MoS_2 and MXene layers increased the sensitivity of the biosensor, we also plotted the relationship between the sensitivity of the biosensor and the RI of the sensing layer (see Figure 5).

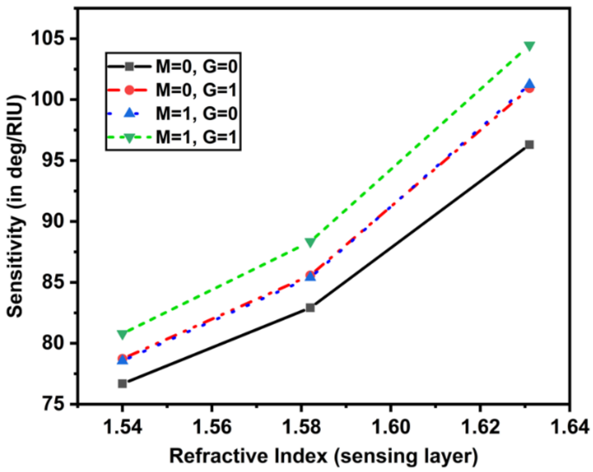

Figure 5. Sensitivity plot w.r.t. the RI of sensing layer (1.54 to 1.64).

It can be seen that as the sensing layer's RI rose from 1.54 to 1.64, the sensitivity rose dramatically. Figure 6A gave the impact of the addition of MoS_2 layers with mono MXene on the sensitivity by varying the RI of the sensing layer. For ($M = 1, G = 1$), ($M = 2, G = 1$), and ($M = 3,\ G = 1$), the sensitivity increased, but in another case ($M = 4,\ G = 1$) the sensitivity increased until 1.58 RI of sensing layer, then the values remained almost constant. The maximum value of sensitivity obtained was 104.471 deg/RIU. A similar trend was obtained for another case, in which the MXene layers varied from 1 to 4 with a monolayer of MoS_2 as shown in Figure 6B. These sensitivity values for both cases have been tabulated in Tables 3 and 4.

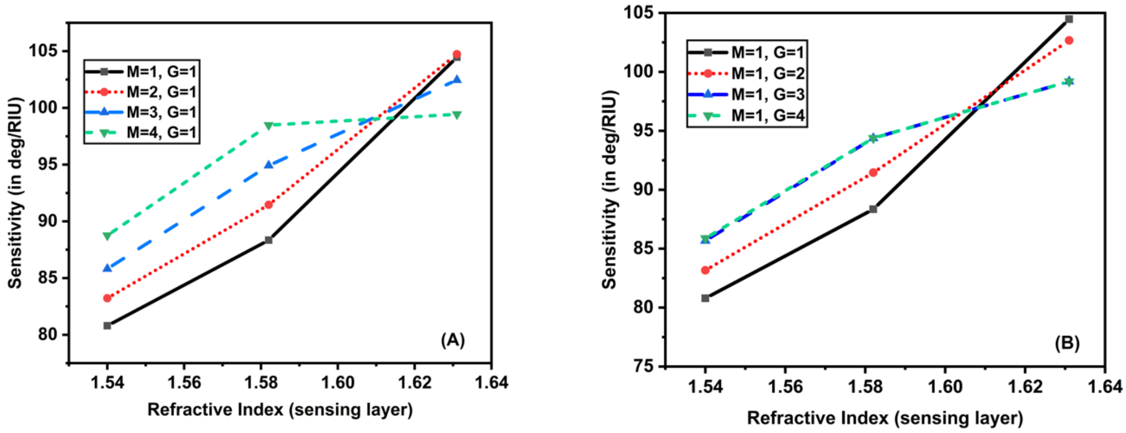

Figure 6. Plot showing sensitivity as a function of RI of sensing layer by varying (**A**) MXene layers with a monolayer of MoS_2, (**B**) MoS_2 layers with a monolayer of MXene.

Table 3. Sensitivity computation when the number of MXene layers varies with a single MoS_2 layer.

RI	Sensitivity (M = 1, G = 1)	Sensitivity (M = 2, G = 1)	Sensitivity (M = 3, G = 1)	Sensitivity (M = 4, G = 1)
1.33	-	-	-	-
1.54	80.795 deg/RIU	83.219 deg/RIU	85.814 deg/RIU	88.757 deg/RIU
1.582	88.345 deg/RIU	91.460 deg/RIU	94.920 deg/RIU	98.484 deg/RIU
1.631	104.471 deg/RIU	104.744 deg/RIU	102.458 deg/RIU	99.441 deg/RIU

Table 4. Sensitivity computation when the number of MoS_2 layers varies with a single MXene layer.

RI	Sensitivity (M = 1, G = 1)	Sensitivity (M = 1, G = 2)	Sensitivity (M = 1, G = 3)	Sensitivity (M = 1, G = 4)
1.33	-	-	-	-
1.54	80.795 deg/RIU	83.166 deg/RIU	85.680 deg/RIU	85.880 deg/RIU
1.582	88.345 deg/RIU	91.452 deg/RIU	94.380 deg/RIU	94.380 deg/RIU
1.631	104.471 deg/RIU	102.671 deg/RIU	99.189 deg/RIU	99.196 deg/RIU

3.1. Detection

This section has theoretically investigated the detection of tooth particles using an SPR sensor. The tooth particles' concentration (C) was added to the sensing layer using the input unit of the flowcell. The concentration added amounts were 0 nm, 25 nm, 50 nm, 100 nm, and 200 nm. Adding these concentrations resulted in an alteration in the RI of the sensing layer. These RI changed in response to the amount of concentration added, giving rise to different SPR curves at different incident angles (Figure 7).

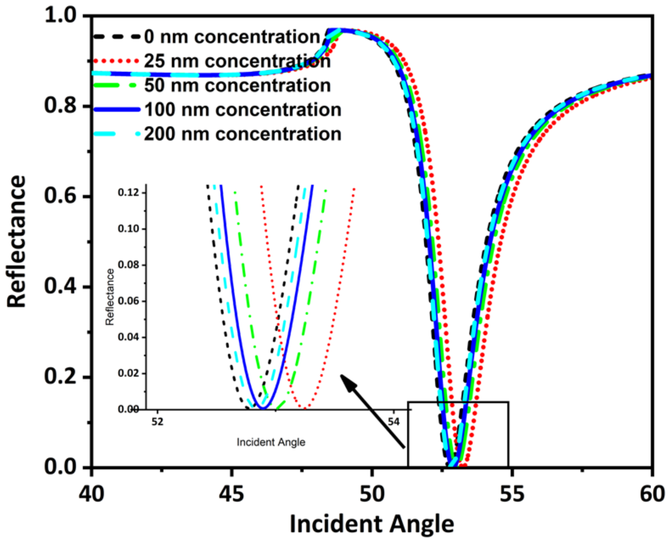

Figure 7. Reflectance and incident angle graph for different detectable targets.

The value of minimum reflectance and incident angle for these concentrations has been shown here using Table 5.

Table 5. R_{min} and incident angle values for different target concentrations.

Concentration Added (nM)	Minimum Reflectance (R_{min})	Incident Angle
0 nM, immobilizer probe	0.000712	52.778 deg
25 nM, detectable target	0.000717	53.241 deg
50 nM detectable target	0.000715	53.009 deg
100 nM, detectable target	0.000713	52.893 deg
200 nM, detectable target	0.000712	52.835 deg

The performance of the existing SPR work with the present study has been summarized in Table 6. As the sensitivity of an SPR biosensor is the most important parameter for evaluation of its performance, a comparison is made on its basis. The wavelength considered was 632.8 or 633 nm.

Table 6. Performance comparison for current work with existing SPR literatures.

References	Design	Sensitivity
Present study	Prism/Ag/MoS_2/MXene	104.744 deg/RIU
[53]	Prism/Au/graphene/Affinity layer	33.98 deg/RIU
[54]	Prism/Ag/Au	54.84 deg/RIU
[55]	Prism/Airgap/Ti/Ag/Au/InP	70.90 deg/RIU
[56]	Prism/Au/graphene/MoS_2	89.29 deg/RIU

3.2. Electric Field Analysis

We used the electric field distribution of the suggested BK7/Ag/MoS_2/MXene sensor construction at a resonance angle to further demonstrate the significant SPR excitation at 52.835 degrees and at analyte 1.631 in Figure 8. As can be observed, the sensing surface produced a considerable electric field augmentation, and the target biomolecules were present in the sensing medium where the electric field strength exponentially diminished [53]. The field strength indicating a larger interaction volume of the field in the sensing. Therefore, while utilising our suggested sensor, the electric probing field close to the MXene layer [57] was very strong and highly sensitive to biomolecule interactions. Similar to few optical sensors [58,59], the proposed sensor was promising for betterment aids in dental applications.

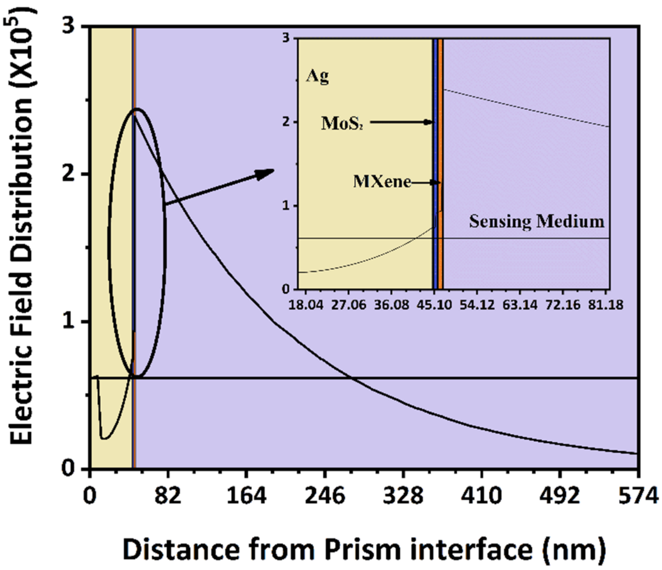

Figure 8. Electric field distribution plot along the direction normal to BK7 prism base indicating the evanescent wave at sensing boundary.

4. Conclusions

The modified Kretschmann configuration was proposed to measure disease in the human teeth, employing Ag, MXene, and the MoS_2 layer. MXene was a 2D material used in the sensor to improve the performance and also work as a protective layer for the Ag to prevent oxidation. MoS_2 was enhancing the bio-interaction ability of the sensor. The designed hybrid biosensor was highly sensitive, and a sensitivity of 104.744 deg/RIU had been observed.

Author Contributions: Conceptualization: M.K.A., V.D., A.N., R.N., M.U.Z., K.K.G., R.B., M.S.M., A.K.N. and H.A.; methodology: V.D., A.N. and R.N.; software: V.D., A.N. and R.N.; validation: V.D., A.N. and R.N.; formal analysis: V.D., A.N. and R.N.; investigation: V.D., A.N. and R.N.; resources: V.D., A.N. and R.N.; data curation: V.D., A.N. and R.N.; writing—original draft preparation: M.K.A., V.D., A.N., R.N., M.U.Z., K.K.G., R.B., M.S.M., A.K.N. and H.A.; writing—review and editing: M.K.A., V.D., A.N., R.N., M.U.Z., K.K.G., R.B., M.S.M., A.K.N. and H.A.; visualization: M.K.A. and V.D.; supervision: M.K.A. and V.D.; project administration: M.K.A. and V.D.; funding acquisition: M.K.A. All authors have read and agreed to the published version of the manuscript.

Funding: Deanship of Scientific Research at Jouf University, Grant No. DSR2022-RG-0158.

Data Availability Statement: All data are available within the manuscript.

Conflicts of Interest: The authors declare no conflict of interest.

References

1. Akib, T.; Mou, S.; Rahman, M.; Rana, M.; Islam, R.; Mehedi, I.; Mahmud, M.; Kouzani, A. Design and numerical analysis of a graphene-coated SPR biosensor for rapid detection of the novel coronavirus. *Sensors* **2021**, *21*, 3491. [CrossRef] [PubMed]
2. Gao, Y.; Xin, Z.; Zeng, B.; Gan, Q.; Cheng, X.; Bartoli, F.J. Plasmonic interferometric sensor arrays for high-performance label-free biomolecular detection. *Lab Chip* **2013**, *13*, 4755–4764. [CrossRef] [PubMed]
3. Chabot, V.; Miron, Y.; Grandbois, M.; Charette, P.G. Long range surface plasmon resonance for increased sensitivity in living cell biosensing through greater probing depth. *Sens. Actuators B Chem.* **2012**, *174*, 94–101. [CrossRef]
4. Yang, X.; Yuan, Y.; Dai, Z.; Liu, F.; Huang, J. Optical property and adsorption isotherm models of glucose sensitive membrane based on prism SPR sensor. *Sens. Actuators B Chem.* **2016**, *237*, 150–158. [CrossRef]

5. Hou, D.; Ji, X.; Luan, N.; Song, L.; Hu, Y.; Luo, M.; He, J.; Bai, Z.; Bai, Z.; Liu, J. Surface Plasmon Resonance Sensor Based on Double-Sided Polished Microstructured Optical Fiber with Hollow Core. *IEEE Photonic J.* **2021**, *13*, 1–8. [CrossRef]
6. Sahu, S.; Ali, J.; Yupapin, P.P.; Singh, G. Porous Silicon Based Bragg-Grating Resonator for Refractive Index Biosensor. *Photonic Sens.* **2018**, *8*, 248–254. [CrossRef]
7. Homola, J. Surface plasmon resonance sensors for detection of chemical and biological species. *Chem. Rev.* **2008**, *108*, 462–493. [CrossRef]
8. Karki, B.; Pal, A.; Singh, Y.; Sharma, S. Sensitivity enhancement of surface plasmon resonance sensor using 2D material barium titanate and black phosphorus over the bimetallic layer of Au, Ag, and Cu. *Opt. Commun.* **2021**, *508*, 127616. [CrossRef]
9. Kretschmann, E.; Raether, H. Radiative decay of non-radiative surface plasmons by light. *Z. Nat.* **1968**, *23*, 2135–2136.
10. Karki, B.; Uniyal, A.; Sharma, T.; Pal, A.; Srivastava, V. Indium phosphide and black phosphorus employed surface plasmon resonance sensor for formalin detection: Numerical analysis. *Opt. Eng.* **2022**, *61*, 017101. [CrossRef]
11. Kashyap, R.; Chakraborty, S.; Zeng, S.; Swarnakar, S.; Kaur, S.; Doley, R.; Mondal, B. Enhanced biosensing activity of bimetallic surface plasmon resonance sensor. *Photonics* **2019**, *6*, 108. [CrossRef]
12. Uniyal, A.; Chauhan, B.; Pal, A.; Singh, Y. Surface plasmon biosensor based on Bi_2Te_3 antimonene heterostructure for the detection of cancer cells. *Appl. Opt.* **2022**, *61*, 3711–3719. [CrossRef]
13. Deng, Y.; Cao, G.; Yang, H.; Zhou, X.; Wu, Y. Dynamic Control of Double Plasmon-Induced Transparencies in Aperture-Coupled Waveguide-Cavity System. *Plasmonics* **2017**, *13*, 345–352. [CrossRef]
14. Deng, Y.; Cao, G.; Wu, Y.; Zhou, X.; Liao, W. Theoretical Description of Dynamic Transmission Characteristics in MDM Waveguide Aperture-Side-Coupled with Ring Cavity. *Plasmonics* **2015**, *10*, 1537–1543. [CrossRef]
15. Datta, S.; Modak, B.; Chaki, N. A Complete Review on Dental Carious Lesion Detection Methods and its Challenges. *Acta Sci. Dent. Sci.* **2019**, *3*, 74–81. [CrossRef]
16. Wu, L.; Jia, Y.; Jiang, L.; Guo, J.; Dai, X.; Xiang, Y.; Fan, D. Sensitivity Improved SPR Biosensor Based on the MoS2/Graphene–Aluminum Hybrid Structure. *J. Light Technol.* **2016**, *35*, 82–87. [CrossRef]
17. Kim, N.-H.; Choi, M.; Kim, T.W.; Choi, W.; Park, S.Y.; Byun, K.M. Sensitivity and stability enhancement of surface plasmon resonance biosensors based on a large-area Ag/MoS_2 substrate. *Sensors* **2019**, *19*, 1894. [CrossRef]
18. Lin, Z.; Jiang, L.; Wu, L.; Guo, J.; Dai, X.; Xiang, Y.; Fan, D. Tuning and Sensitivity Enhancement of Surface Plasmon Resonance Biosensor with Graphene Covered Au-MoS 2-Au Films. *IEEE Photonic J.* **2016**, *8*, 1–8. [CrossRef]
19. Kumar, A.; Yadav, A.K.; Kushwaha, A.S.; Srivastava, S. A comparative study among WS2, MoS2 and graphene based surface plasmon resonance (SPR) sensor. *Sens. Actuators Rep.* **2020**, *2*, 100015. [CrossRef]
20. Karki, B.; Uniyal, A.; Chauhan, B.; Pal, A. Sensitivity enhancement of a graphene, zinc sulfide-based surface plasmon resonance biosensor with an Ag metal configuration in the visible region. *J. Comput. Electron.* **2022**, *21*, 445–452. [CrossRef]
21. Nurrohman, D.T.; Chiu, N.-F. Surface Plasmon Resonance Biosensor Performance Analysis on 2D Material Based on Graphene and Transition Metal Dichalcogenides. *ECS J. Solid State Sci. Technol.* **2020**, *9*, 115023. [CrossRef]
22. Pal, A.; Jha, A. A theoretical analysis on sensitivity improvement of an SPR refractive index sensor with graphene and barium titanate nanosheets. *Optik* **2021**, *231*, 166378. [CrossRef]
23. Zhao, Y.; Gan, S.; Zhang, G.; Dai, X. High sensitivity refractive index sensor based on surface plasmon resonance with topological insulator. *Results Phys.* **2019**, *14*, 102477. [CrossRef]
24. Sathya, N.; Karki, B.; Rane, K.P.; Jha, A.; Pal, A. Tuning and Sensitivity Improvement of Bi-Metallic Structure-Based Surface Plasmon Resonance Biosensor with 2-D ε-Tin Selenide Nanosheets. *Plasmonics* **2022**, *17*, 1001–1008. [CrossRef]
25. Srivastava, T.; Jha, R. Black Phosphorus: A New Platform for Gaseous Sensing Based on Surface Plasmon Resonance. *IEEE Photonic Technol. Lett.* **2018**, *30*, 319–322. [CrossRef]
26. Singh, Y.; Raghuwanshi, S.K. Sensitivity Enhancement of the Surface Plasmon Resonance Gas Sensor with Black Phosphorus. *IEEE Sens. Lett.* **2019**, *3*, 1–4. [CrossRef]
27. Wu, L.; Guo, J.; Wang, Q.; Lu, S.; Dai, X.; Xiang, Y.; Fan, D. Sensitivity enhancement by using few-layer black phosphorus-graphene/TMDCs heterostructure in surface plasmon resonance biochemical sensor. *Sens. Actuators B Chem.* **2017**, *249*, 542–548. [CrossRef]
28. Bijalwan, A.; Rastogi, V. Gold–aluminum-based surface plasmon resonance sensor with a high quality factor and figure of merit for the detection of hemoglobin. *Appl. Opt.* **2018**, *57*, 9230–9237. [CrossRef]
29. Karki, B.; Sharma, S.; Singh, Y.; Pal, A. Sensitivity Enhancement of Surface Plasmon Resonance Biosensor with 2-D Franckeite Nanosheets. *Plasmonics* **2021**, *17*, 71–78. [CrossRef]
30. Liu, L.; Zhang, X.; Zhu, Q.; Li, K.; Lu, Y.; Zhou, X.; Guo, T. Ultrasensitive detection of endocrine disruptors via superfine plasmonic spectral combs. *Light Sci. Appl.* **2021**, *10*, 181. [CrossRef]
31. Sun, J.; Du, H.; Chen, Z.; Wang, L.; Shen, G. MXene quantum dot within natural 3D watermelon peel matrix for biocompatible flexible sensing platform. *Nano Res.* **2021**, *15*, 3653–3659. [CrossRef]
32. Du, X.; Tian, W.; Pan, J.; Hui, B.; Sun, J.; Zhang, K.; Xia, Y. Piezo-phototronic effect promoted carrier separation in coaxial p-n junctions for self-powered photodetector. *Nano Energy* **2021**, *92*, 106694. [CrossRef]
33. Liu, W.; Zheng, Y.; Wang, Z.; Wang, Z.; Yang, J.; Chen, M.; Qi, M.; Rehman, S.U.; Shum, P.P.; Zhu, L.; et al. Ultrasensitive Exhaled Breath Sensors Based on Anti-Resonant Hollow Core Fiber with In Situ Grown ZnO-Bi_2O_3 Nanosheets. *Adv. Mater. Interfaces* **2021**, *8*, 2001978. [CrossRef]

34. Shangguan, Q.; Chen, Z.; Yang, H.; Cheng, S.; Yang, W.; Yi, Z.; Wu, X.; Wang, S.; Yi, Y.; Wu, P. Design of Ultra-Narrow Band Graphene Refractive Index Sensor. *Sensors* **2022**, *22*, 6483. [CrossRef]
35. Bu, W.; Wu, Z.; Shum, P.P.; Shao, X.; Pu, J. Sensitivity Enhanced Refractive Index Fiber Sensor Based on Long-Range Surface Plasmon Resonance in SiO_2-Au-TiO_2 Heterostructure. *Photonics* **2021**, *8*, 379. [CrossRef]
36. Naguib, M.; Mochalin, V.N.; Barsoum, M.W.; Gogotsi, Y. 25th anniversary article: MXenes: A new family of two-dimensional materials. *Adv. Energy Mater.* **2014**, *26*, 992–1005. [CrossRef]
37. Pandey, P.S.; Singh, Y.; Raghuwanshi, S.K. Theoretical analysis of the LRSPR sensor with Enhance FOM for Low Refractive Index Detection using MXene and Fluorinated Graphene. *IEEE Sens. J.* **2021**, *21*, 23979–23986. [CrossRef]
38. Anasori, B.; Lukatskaya, M.R.; Gogotsi, Y. 2D metal carbides and nitrides (MXenes) for energy storage. *Nat. Rev. Mater.* **2017**, *2*, 16098. [CrossRef]
39. Miranda, A.; Halim, J.; Lorke, A.; Barsoum, M.W. Rendering $Ti_3C_2T_x$ (MXene) monolayers visible. *Mater. Res. Lett.* **2017**, *5*, 322–328. [CrossRef]
40. Uniyal, A.; Chauhan, B.; Pal, A.; Srivastava, V. InP and graphene employed surface plasmon resonance sensor for measurement of sucrose concentration: A numerical approach. *Opt. Eng.* **2022**, *61*, 057103. [CrossRef]
41. Johnson, P.B.; Christy, R.W. Optical Constant of the Nobel Metals. *Phys. Rev. B* **1972**, *6*, 4370–4379. [CrossRef]
42. Karki, B.; Trabelsi, Y.; Uniyal, A.; Pal, A. Zinc sulfide, silicon dioxide, and black phosphorus based ultra-sensitive surface plasmon biosensor. *Opt. Quantum Electron.* **2022**, *54*, 107. [CrossRef]
43. Liu, L.; Wang, M.; Jiao, L.; Wu, T.; Xia, F.; Liu, M.; Kong, W.; Dong, L.; Yun, M. Sensitivity enhancement of a graphene–barium titanate-based surface plasmon resonance biosensor with an Ag–Au bimetallic structure in the visible region. *JOSA B* **2019**, *36*, 1108–1116. [CrossRef]
44. Singh, Y.; Paswan, M.K.; Raghuwanshi, S.K. Sensitivity Enhancement of SPR Sensor with the Black Phosphorus and Graphene with Bi-layer of Gold for Chemical Sensing. *Plasmonics* **2021**, *16*, 1781–1790. [CrossRef]
45. Gwon, H.R.; Lee, S.H. Spectral and angular responses of surface plasmon resonance based on the kretschmann prism configuration. *Mater. Trans.* **2010**, *51*, 1150–1155. [CrossRef]
46. Srivastava, S.K.; Verma, R.; Gupta, B.D. Theoretical modeling of a self-referenced dual mode SPR sensor utilizing indium tin oxide film. *Opt. Commun.* **2016**, *369*, 131–137. [CrossRef]
47. Mostufa, S.; Paul, A.K.; Chakrabarti, K. Detection of hemoglobin in blood and urine glucose level samples using a graphene-coated SPR based biosensor. *OSA Contin.* **2021**, *4*, 2164–2176. [CrossRef]
48. Hossain, B.; Rana, M.; Abdulrazak, L.F.; Mitra, S.; Rahman, M. Design and analysis of graphene–MoS_2 hybrid layer based SPR biosensor with TiO_2–SiO_2 nano film for formalin detection: Numerical approach. *Opt. Quantum Electron.* **2019**, *51*, 195. [CrossRef]
49. Rahman, M.; Rana, M.; Rahman, S.; Anower, M.; Mollah, A.; Paul, A.K. Sensitivity enhancement of SPR biosensors employing heterostructure of $PtSe_2$ and 2D materials. *Opt. Mater.* **2020**, *107*, 110123. [CrossRef]
50. Mostufa, S.; Akib, T.B.A.; Rana, M.; Islam, R. Highly Sensitive TiO_2/Au/Graphene Layer-Based Surface Plasmon Resonance Biosensor for Cancer Detection. *Biosensors* **2022**, *12*, 603. [CrossRef]
51. Basak, C.; Hosain, K.; Sazzad, A.A. Design and Simulation of a High Sensitive Surface Plasmon Resonance Biosensor for Detection of Biomolecules. *Sens. Imaging* **2019**, *21*, 2. [CrossRef]
52. Shalabney, A.; Abdulhalim, I. Electromagnetic fields distribution in multilayer thin film structures and the origin of sensitivity enhancement in surface plasmon resonance sensors. *Sens. Actuators A Phys.* **2010**, *159*, 24–32. [CrossRef]
53. Verma, A.; Prakash, A.; Tripathi, R. Performance analysis of graphene based surface plasmon resonance biosensors for detection of pseudomonas-like bacteria. *Opt. Quantum Electron.* **2014**, *47*, 1197–1205. [CrossRef]
54. Xia, L.; Yin, S.; Gao, H.; Deng, Q.; Du, C. Sensitivity Enhancement for Surface Plasmon Resonance Imaging Biosensor by Utilizing Gold–Silver Bimetallic Film Configuration. *Plasmonics* **2011**, *6*, 245–250. [CrossRef]
55. Rouf, H.K.; Haque, T. Performance enhancement of Ag-Au bimetallic surface plasmon resonance biosensor using InP. *Prog. Electromagn. Res. M* **2018**, *76*, 31–42. [CrossRef]
56. Rahman, M.S.; Anower, S.; Hasan, R.; Hossain, B.; Haque, I. Design and numerical analysis of highly sensitive Au-MoS2-graphene based hybrid surface plasmon resonance biosensor. *Opt. Commun.* **2017**, *396*, 36–43. [CrossRef]
57. Ramanavicius, S.; Ramanavicius, A. Progress and Insights in the Application of MXenes as New 2D Nano-Materials Suitable for Biosensors and Biofuel Cell Design. *Int. J. Mol. Sci.* **2020**, *21*, 9224. [CrossRef]
58. Tabrizi, M.A.; Ferre-Borrull, J.; Marsal, L.F. Advances in Optical Biosensors and Sensors Using Nanoporous Anodic Alumina. *Sensors* **2020**, *20*, 5068. [CrossRef]
59. Li, K.; Zhou, W.; Zeng, S. Optical Micro/Nanofiber-Based Localized Surface Plasmon Resonance Biosensors: Fiber Diameter Dependence. *Sensors* **2018**, *18*, 3295. [CrossRef]